Available online at www.sciencedirect.com

ScienceDirect

Geochimica et Cosmochimica Acta 149 (2015) 115–130

Geochimica et Cosmochimica Acta

www.elsevier.com/locate/gca

Quantitative textural analysis of ilmenite in Apollo 17 high-titanium mare basalts

Patrick H. Donohue *, Clive R. Neal

Department of Civil and Environmental Engineering and Earth Sciences, University of Notre Dame, Notre Dame, IN 46556, USA

Received 20 January 2014; accepted in revised form 1 November 2014; Available online 8 November 2014

Abstract

Quantitative textural analysis is a powerful tool in the investigation of basalt crystallization. We present the first comprehensive crystal size distribution analysis of Apollo 17 high-titanium lunar basalts, with a focus on ilmenite. Crystal size distributions of ilmenite, pyroxene, plagioclase, olivine and armalcolite were determined for 18 high-Ti mare basalt samples from the Apollo 17 mission. A subset of the ilmenite size distribution (size bins of <0.6 mm in length) reflects growth at post-eruption or post-emplacement cooling rates. Growth of these small ilmenite crystals is controlled by cooling rate and not bulk composition or ilmenite abundance. CSD characteristics tied to cooling rate determined by experiments yield estimates of cooling rate in natural samples. Matrix ilmenite grew at rates up to 250 °C/h, while most samples contained phenocrysts that originated in environments cooling at <3 °C/h. Textural characteristics of ilmenite phenocrysts are used to develop a relative stratigraphy for the samples within a lava flow based upon comparisons with terrestrial analogues.
© 2014 Elsevier Ltd. All rights reserved.

1. INTRODUCTION

While titanium is sparse in terrestrial basalts (typically containing 2–3 wt.% bulk rock TiO_2 or less), lunar mare basalts may contain up to 14 wt.% TiO_2 (e.g., Neal and Taylor, 1992), and basaltic mare glasses can contain up to 17 wt.% TiO_2 (e.g., Shearer et al., 1990). As a result, Ti-rich minerals (i.e., ilmenite, armalcolite, and Ti-spinel) play a more pronounced role in the crystallization of lunar basalts compared to terrestrial basalts. Ti-rich spinel can be found as inclusions in olivine, particularly in Type C basalts classified by whole-rock chemistry, but is soon replaced by armalcolite and ilmenite (Papike et al., 1976). In particular, lunar basalts with >6 wt.% TiO_2 ("high-Ti") typically contain more than 10 modal percent ilmenite (*cf.* Papike et al., 1976). Basaltic samples indirectly allow the nature of the lunar interior to be evaluated and crystallization processes are reflected in the morphology and size distribution of major phases. Thin sections of mare basalts are slices of truth, windows into the complex processes visited upon these igneous rocks. Petrographic observations are bolstered by the non-destructive creation of crystal size distributions (CSDs). The robustness of this crystal stratigraphy method has been demonstrated in terrestrial and lunar basalts alike (e.g., Cashman and Marsh, 1988; Day and Taylor, 2007; Hui et al., 2011; O'Sullivan, 2012; Fagan et al., 2013). These previous studies focused on low-Ti basalts where, for example, Hui et al. (2011) showed Apollo 14 chemical groups – interpreted as separate lava flows – had unique plagioclase CSDs reflecting distinct textures and petrogeneses. In the low-Ti mare basalts, ilmenite is a minor phase and was not the focus of study.

The Apollo 11 and Apollo 17 missions returned samples of high-Ti mare basalts and, recently, high-Ti basalts have been described in regolith samples and as breccia clasts from Apollo 16 (Zeigler et al., 2006; Fagan and Neal, 2012, 2014). Apollo 17 basalts make up a larger sample

* Corresponding author. Tel.: +1 (574) 631 4306; fax: +1 (574) 631 9236.

E-mail address: pdonohu1@nd.edu (P.H. Donohue).

http://dx.doi.org/10.1016/j.gca.2014.11.002
0016-7037/© 2014 Elsevier Ltd. All rights reserved.

set and are the more texturally diverse suite, and have been classified both on the basis of chemistry and texture. The five known whole-rock chemical groups (Types A, B1, B2, C, and D; Rhodes et al., 1976; Neal et al., 1990) experienced a similar history of shallow-level fractionation and crystallization following separation from unique sources. There is also a textural continuum ranging from vitrophyric to micro-gabbroic that is independent of whole-rock chemistry. Type D is an exception, as it is defined by one 22-gram sample (79001,2187; Ryder, 1990). Multiple but similar threefold textural classification schemes have been proposed for Apollo 17 high-Ti basalts (Papike et al., 1974; Brown et al., 1975; Warner et al., 1975b; see comparison by Dymek et al., 1975). In this study, the textural naming conventions of Brown et al. (1975) are used, which are: **Type 1A** quenched olivine-porphyritic ilmenite basalt (Fig. 1a); **Type 1B** slower-cooled, olivine-poor (<5 vol.%), plagioclase-poikilitic ilmenite basalt (Fig. 1b); and the relatively rare **Type II** olivine-free, low-Mg ilmenite basalt similar to Apollo 11 low-K type basalt – Brown et al. (1975) describe only two samples with this texture (75035 and 75055). The comparison to Apollo 11 basalts is based solely on major element chemistry of bulk sample analysis. There is a textural continuum between textural Types 1A and 1B, and all three petrographic types are present in each chemical group. The Apollo 17 sample set here includes eight textural Type 1A basalts (fine-grained olivine-porphyritic) and ten textural Type 1B basalts (coarse-grained plagioclase-poikilitic). The sample petrography of textural Type 1A and 1B basalts is summarized below.

The eighteen Apollo 17 high-Ti basalts studied here were collected from various stations over the Apollo 17 landing site (Fig. 2). The numbering convention used has the first digit "7" representing the Apollo *Seven*teen mission and the second number corresponding to the particular station where the sample was acquired. If the second digit is "0" it was collected around the Lunar Module, denoted by the solid white circle in Fig. 2. If the second digit is "1" it was collected at Station 1. If the second digit is >1, the sample was collected at that station or between it and the previous one. Over 120 samples of high-Ti basalt have been described from the Apollo 17 site (Ryder, 1992; Neal and Taylor, 1993b,c; Meyer, 1994). To date 48 Type A, 14 Type B1, 39 Type B2, 7 Type C, and 1 Type D basalts have been defined on the basis of whole-rock chemistry from samples returned by the Apollo 17 mission (e.g., Neal et al., 1990; Donohue, 2013). There are still several coarse grained samples that were originally classified as "Type U" (Rhodes et al., 1976) because a representative whole-rock analysis was not possible.

In high-Ti basalts, ilmenite is an early and prolonged crystallizing phase (e.g., Brown et al., 1975; Dymek et al., 1975; Papike et al., 1976). Thus, the size and distribution of ilmenite should prove valuable in defining crystallization histories. Early studies of high-Ti analogues calibrated

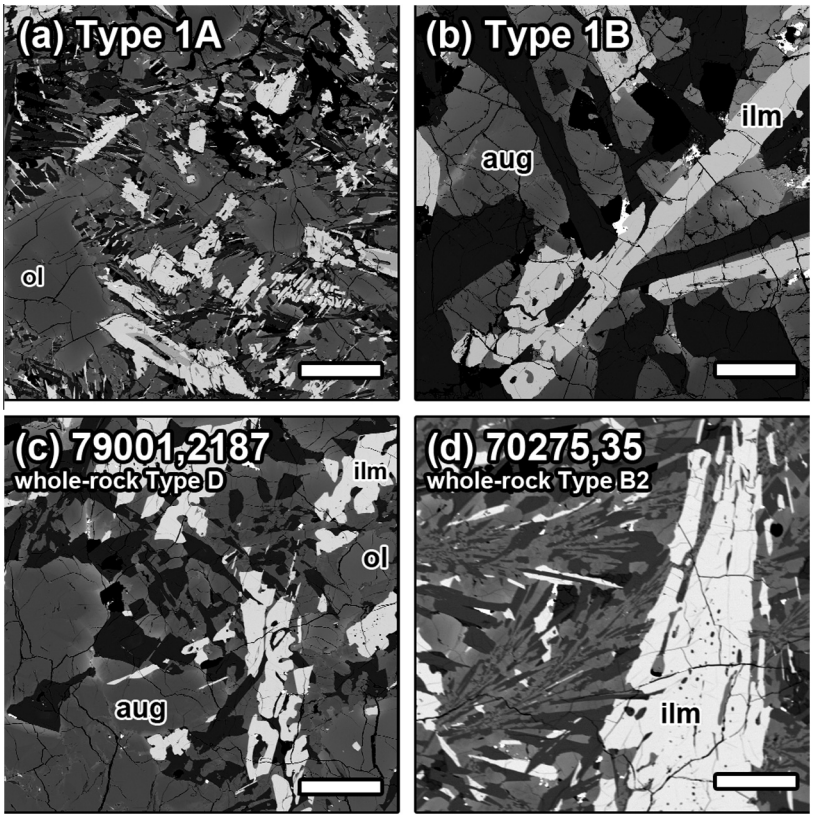

Fig. 1. Representative textures in backscattered electron (BSE) photomicrographs. (a) BSE image of olivine microporphyritic textural Type 1A basalt 79516,9. (b) BSE image of plagioclase poikilitic textural Type 1B basalt 75015,52. (c) BSE image of whole-rock Type D basalt 79001,2187 which has a texture intermediate between textural Types 1A and Type 1B. (d) BSE image of portion of 70275,35 highlighting the variation in ilmenite size in the fine-grained region. Scale bar is 0.2 mm in all images.

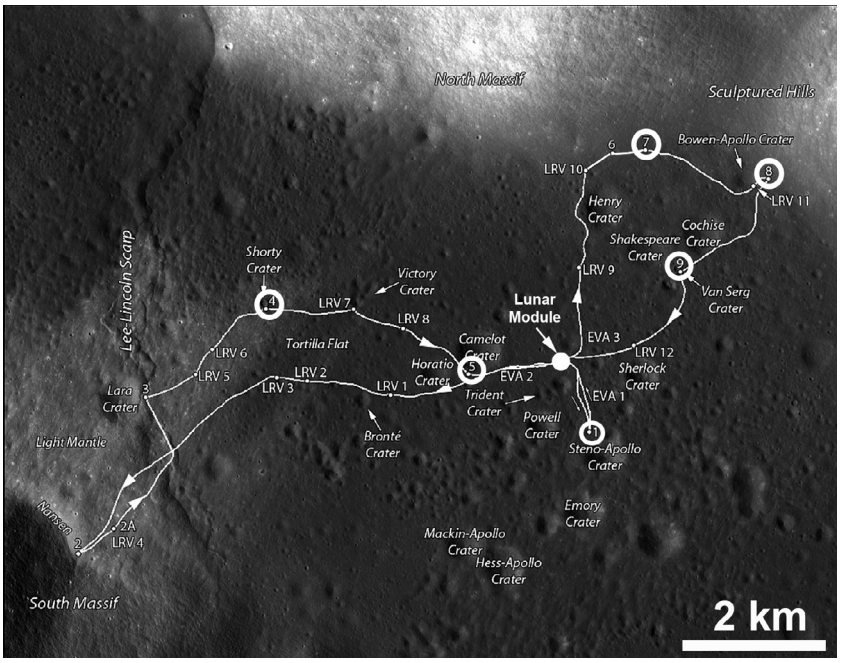

Fig. 2. Apollo 17 traverse map with the stations from which the samples used in this study were collected highlighted by a white circle outline. The Lunar Module is depicted by a solid white circle. Modified from Neal and Taylor (1993a).

observed textural relationships to cooling rates through experimental crystallization studies (Usselman et al., 1975). In this study, we report quantitative petrographic analyses of the major mineral phases in eighteen Apollo 17 high-Ti mare basalts. Textural variation demonstrated by crystal size distribution (CSD) profiles is subsequently linked to experimentally produced textures. These relationships provide information on Apollo 17 high-Ti basalt crystallization that allows us to place samples in terms of lava flow position and cooling history. The main classification used is that of whole-rock chemistry and the textural classification terminology is used to describe samples within a given whole-rock group.

2. SAMPLES AND PETROGRAPHY

The investigated sample set was chosen to cover the compositional diversity of Apollo 17 high-Ti mare basalts (Fig. 1, Table 1) and includes basalts from all Apollo 17 whole-rock chemical groups (four Type A, four Type B1, five Type B2, four Type C, and the sole Type D 79001,2187). The olivine CSD for sample 74275,312 was previously reported by Fagan et al. (2013) as part of a larger olivine textural study. Textures of these samples range from olivine (micro)-porphyritic ($n = 8$) to plagioclase-poikilitic ($n = 9$), to allotriomorphic granular (78575). Two additional ilmenite CSDs were made for 70275,35, which contains two textural types: the dominant texture is variolitic but it also contains a coarser subophitic region.

Textural Type 1A (Brown et al., 1975) olivine-porphyritic basalts are typified by a fine-grained matrix (<1 mm) with phenocrysts of olivine (0.4–1.5 mm) and ilmenite (up to 3 mm long, typically 0.5–1 mm). Olivine phenocrysts (0.4–1.5 mm) are present as discrete grains, while smaller crystals (<0.3 mm) may be discrete or form the cores of augite crystals. Ilmenite phenocrysts are commonly elongate and many exhibit "sawtooth" margins (Fig. 1a), indicative of rapid cooling (Papike et al., 1974). Armalcolite occurs as discrete euhedral grains in vitrophyric samples 71157 and 74235, sometimes as inclusions within olivine, or with thin (<0.1 mm) ilmenite mantles. Where less abundant, armalcolite is found as ovoid grains (<0.1 mm) in large pyroxenes (~1 mm), or with thicker (0.1–0.25 mm) ilmenite mantles. Euhedral Cr-ulvöspinel grains (~0.1 mm) are present as inclusions in olivine and, less frequently, pyroxene. Pyroxene has a tendency to cluster, with individual crystals up to 0.5 mm long, but it is generally smaller, anhedral, and often interstitial. Plagioclase is mostly interstitial and typically forms fan spherulites with pyroxene. Fan spherulites commonly form from intergrowths of ilmenite (acicular crystals up to 0.8 mm long), plagioclase and pyroxene. Phenocrysts are common nucleation sites and in some cases have interfered with spherulite growth (i.e., truncation, deformation), possibly indicating crystal transport during rapid cooling. Trace amounts of troilite, Fe-metal and silica are present as interstitial phases.

Textural Type 1B plagioclase-poikilitic basalts are composed primarily of medium- to coarse-grained pyroxene, plagioclase, and ilmenite as major phases. Olivine is absent from samples 71509, 75015 and 78575. Where present, olivine forms crystals subhedral to anhedral (<0.3 mm) as cores to augite, or is poikilitically enclosed by plagioclase. Rare larger (0.7–3 mm) olivine crystals are found in samples 74255 and 79001 (Fig. 1c). Ilmenite tends to be either equant or elongated and typically ~0.5 mm on the long axis, but is 2–3 mm long in some samples. Ilmenite

Table 1
Textural type and selected bulk composition of high-Ti basalts.

Sample	Textural type	Chemical type	MgO (wt.%)	TiO_2 (wt.%)	WR Reference
70135,64	1B	A	9.29	13.34	[1]
71048,6	1A	A	8	12.9	[2]
74235,60	1A	A	8.35	12.17	[1]
75015,52	1B	A	6.2	9.56	[1]
70315,27	1B	B1	10	13.1	[3]
71557,7	1B	B1	8.5	13	[4]
75075,86	1B	B1	9.49	13.45	[1]
78575,10	1B	B1	7.5	11.8	[4]
70275,35	1A	B2	6.09	11.9	[1]
71035,32	1B	B2	7.98	13.06	[1]
71157,8	1A	B2	7.5	12.6	[2]
77516,30	1A	B2	9.4	13.7	[4]
79516,9	1A	B2	8	12.3	[3]
71509,5	1B	C	10.3	13.7	[5]
74255,55	1B	C	10.5	12.17	[1]
74275,312	1A	C	10.36	12.7	[1]
75115,4	1A	C	9.3	12.6	[5]
79001,2187	1B	D	10.9	9.9	[6]

[1] Rhodes et al. (1976); [2] Neal et al. (1990); [3] Warner et al. (1979); [4] Warner et al. (1975b); [5] Warner et al. (1975a); [6] Ryder (1990).

morphology varies depending on cooling rate, and ranges from acicular to tabular with decreasing cooling rate. As the most abundant phase, pyroxene tends to be larger and form crystals several millimeters in size. In some samples (e.g., 74255 and 70315), armalcolite and olivine (where present) are found only as inclusions within the largest (>2.5 mm) pyroxenes. Troilite, Fe-metal, and anhedral silica form interstitial phases.

Many more photomicrographs of these samples were taken beyond what is shown in Fig. 1. These can be found on-line at http://www.lpi.usra.edu/lunar/samples/atlas/thin_sections/.

3. THE CRYSTAL SIZE DISTRIBUTION (CSD) AND SPATIAL DISTRIBUTION PROFILE (SDP) METHODS

Crystal size distributions are a quantitative method of defining the texture of specific mineral species in an igneous rock. The shape and interpretation of CSD curves are useful in determining initial nucleation density, nucleation rate, growth rate, and whether the magma system was closed or open (Cashman and Marsh, 1988; Marsh, 1998). The typical CSD is a histogram of corrected crystal size versus natural log of population density $ln(n)$ (Fig. 3a and b). A line connecting peaks of the size bins is a function of growth rate (G) and residence time (τ):

$$n = n_0 \exp(-L/G\tau) \quad (1)$$

where n_0 is initial nucleation density (in crystals per unit area). Thus, a linear CSD results from uninterrupted nucleation and growth rates (constant G and τ) during crystallization. Curved CSDs (Fig. 3a) can result from multiple processes, including magma mixing, textural coarsening, crystal settling (fractionation or accumulation), changes in cooling rate or equilibrium state (e.g., assimilation processes), or other open-system processes (Marsh, 1988, 1998). Processes affecting G and τ may also result in "kinked" CSDs (Fig. 3b).

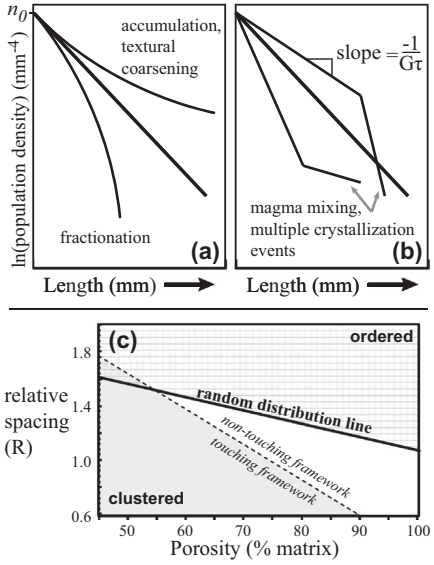

Fig. 3. (a and b) Idealized crystal size distributions and potential causes of change to CSD profiles that may result in (a) curved or (b) kinked CSDs (modified after Marsh (1998)). The slope is a function of growth rate (G) and residence time (τ). (c) Spatial distribution fields show the derived regions of importance for textural interpretations (modified after Jerram et al. (1996, 2003)).

The SDPs of minerals also reflect magmatic processes (e.g., crystal nucleation and growth, flow settling, flow orientation). The relative ordering and frameworks of crystal phases can be assessed by comparison with the distribution of randomly packed spheres (Jerram et al., 1996, 2003). The R-value is defined as

$$R = \frac{2\sqrt{\rho}\sum r}{n} \quad (2)$$

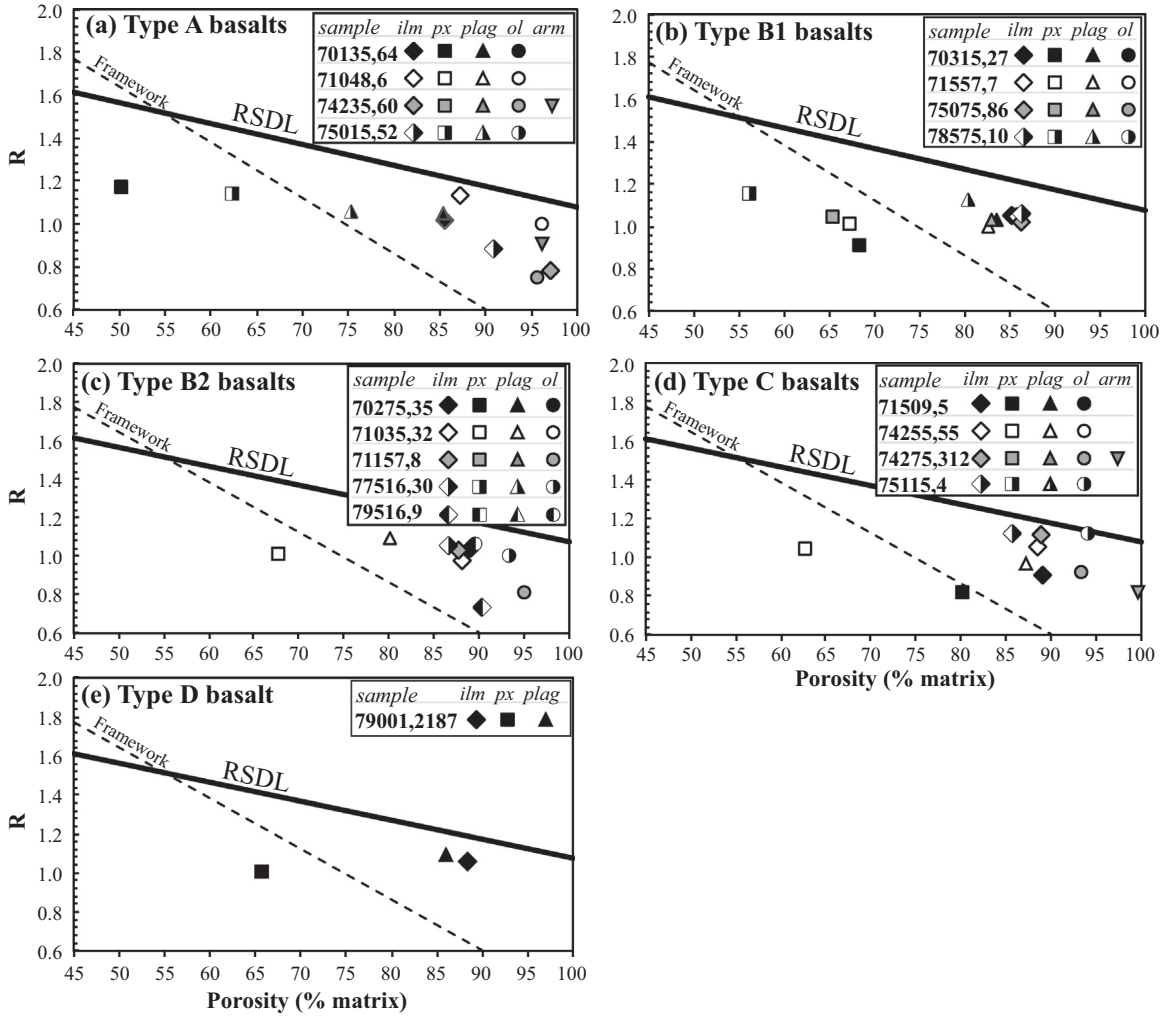

Fig. 4. Spatial Distribution Profiles for the Apollo 17 high-Ti basalts. (a) Type A basalts. Note plagioclase approaches the Touching Framework Line in sample 75015,52. (b) Type B1 basalts, where ilmenite, plagioclase and pyroxene form clusters with the exception of allotriomorphic-granular sample 78575,10. (c) Type B2 basalts. For 70275,35, the *R*-values of the fine (1.09) and coarse (1.00) regions plot within the symbol size of the overall sample ($R = 1.04$). (d) Type C basalts. (e) Type D basalt 79001,2187. RSDL = Random Sphere Distribution Line. Adapted from Jerram et al. (1996, 2003).

where ρ is the number density (in crystals per unit area) of the observed distribution, r is the nearest neighbor (center-to-center) distances, and n is the total number of individuals measured (Jerram et al., 1996). By comparing the *R*-value to porosity (percent matrix), it is possible to distinguish touching from non-touching frameworks, as well as the relative ordering or clustering of phases (Fig. 3c). In conjunction with CSDs and mineral chemistry, SDPs can discern between effects of crystal nucleation and growth, magma mixing (Martin et al., 2006), and relative position in igneous flows and intrusions (Jerram et al., 2003, 2010; Day and Taylor, 2007).

Quantitative CSD and SDP analyses were performed, where possible, for ilmenite, armalcolite, plagioclase, pyroxene, and olivine on mosaics of thin section digital photomicrographs at 5× magnification. Backscattered electron images and X-ray maps of select samples were also used as reference when necessary. Crystals were identified and outlined with a drawing tablet in Adobe© *Photoshop*©. Ilmenite and armalcolite were identified in reflected light. Plagioclase, pyroxene and olivine were identified using plane-polarized and cross-polarized views. These methods allowed touching crystals and glomerocrysts to be identified and separated. Crystal sizes for many phases extended to sizes smaller than could be reliably identified (<~0.05 mm) from photomicrograph resolution. At the 5× magnification used, images have resolutions of ~33 pixels per 0.05 mm. The centroid X and Y coordinates, major and minor axis lengths and area of crystal phases were calculated in the image-processing program *ImageJ* (Rasband, 1997). *CSDSlice* (ver. 4) (Morgan and Jerram, 2006) converted the 2D thin section crystal dimensions into their most-probable 3D crystal dimensions. These calculated parameters, in addition to roundness and fabric, were used to generate CSDs with the *CSDCorrections* program (v. 1.3.9; Higgins, 2000). The roundness used was an average of best-fit ellipse shapes, and a massive fabric was used as no foliation or flow features were apparent. CSDs were

corrected for volumetric phase abundance as the program tended to overestimate mineral percentages by a factor of two or more for acicular crystals. This was accomplished by constraining the final volumetric abundance to equal that calculated in the thin section.

Eq. (1) can only be applied on a classic CSD diagram of ln(population density) *versus* corrected size if the slope and intercept are linear. The program *CSDCorrections* tests the linearity of a CSD profile by calculating goodness of fit (Q) of the data (including error) to a straight line. Values of $Q > 0.1$ are preferred, and $Q > 0.001$ is sublinear as curved CSD profiles give Q-values that are typically orders of magnitude lower than one (Higgins, 2006). This allows calculation of a slope and an intercept for CSDs determined to be linear ($Q > 0.1$) or sub-linear (Q between 0.001 and 0.1). For concave CSDs ($Q < 0.001$), the slope and intercept of both the smallest and largest portions of the profile are calculated.

The number of phases for which CSDs can be generated is limited by crystal size and the population of crystals required to yield a good statistical fit to a CSD model. Therefore, CSDs are not produced for all phases present in a given sample. Morgan and Jerram (2006) recommended >250 crystals for more acicular forms, with less ($n > 75$) required for tabular crystals.

4. RESULTS

Quantitative textural analysis yielded between 77 and 7958 crystals for phases traced (Table 2). Size bins containing less than three crystals were not statistically significant and were not included in subsequent CSD calculations (italicized values in Table 2). Ilmenite was the sole phase for which a CSD was generated in every thin section (18 samples). For other phases, textural type (fast-cooled Type 1A versus slow-cooled Type 1B) was a good indicator for which phases could be quantified in a given thin section. Pyroxene and plagioclase CSDs were determined for all Type 1B basalts, with the exception of 71509,5. A pyroxene CSD was generated for 71509,5, but plagioclase was not abundant enough for a CSD as the thin section comprised only four small (<10 mm^2) fragments. The large, poikilitic nature of plagioclase in 71509,5 resulted in many crystals touching the edge, so that they could not be included in the CSD analysis as they probably were not whole crystals. Olivine CSDs were made for all Type 1B basalts except 70275,35, which did not contain enough olivine for analysis. Armalcolite CSDs were determined only for textural Type 1A samples 74235,60 and 74275,312. In most CSDs from each phase there was a downturn in the CSD profile at small (<~0.1 mm) crystal size bins. Two lines of evidence supported this downturn as being an artifact of the tracing process, namely (1) the downturn occurred at similar sizes for all phases, and (2) there was larger uncertainty in calculated population densities. This lower limit of resolution was similar to that of other CSD studies (Hui et al., 2011; Fagan et al., 2013).

Spatial distribution profile R-values defined a relatively narrow range ($R = 0.73$ to 1.17) for a relatively large range of porosity values (percent matrix) for all phases (Fig. 4). Pyroxene in textural Type 1B basalts formed a connected framework as it plotted below the Touching Framework Line and Random Sphere Distribution Line (RSDL). This might be expected, as pyroxene was the most abundant phase in textural Type 1B samples (35–50% by area). All other examined phases from typical basalts were in the field of a clustered, non-touching framework. Clustering of phases (Fig. 4) is a common feature of phenocryst SDPs in igneous rocks (e.g., Jerram et al., 2003). The distribution in Fig. 4 also suggested accumulation of phases was not significant in the Apollo 17 basalts studied here. Accumulation of phases would be apparent by a deviation in the SDP from other similar phase SDPs, and toward or to the left of the Touching Framework Line. The lower R-values of olivine relative to ilmenite in a given sample may reflect the ability of early-formed olivine to cluster in a relatively lower-viscosity melt prior to entrainment in a cooling crystal mush.

4.1. Ilmenite CSDs

The total number of ilmenite crystals traced per thin section (147–7958 crystals) varied by thin section size, ilmenite size, and volumetric abundance. Ilmenite morphology was wide-ranging, from equigranular blocky, euhedral to anhedral laths, acicular, and occasionally formed with "sawtooth" margins. This variety was reflected by best-fit 3D shape parameters (short:intermediate:long) from *CSDSlice*, which ranged from 1:1.5:2.0 (blocky) to 1:6:10 (platy) to 1:1.9:10 (acicular) (Table 3). Ilmenite CSD profiles exhibited a range in slope (from linear to concave upward) and maximum extent (0.53–7.89 mm) (Fig. 5). There was no apparent co-variation of slope with chemical groups. However, all textural Type 1A basalts had higher population densities of small crystals (<~0.6 mm) compared to textural Type 1B basalts (Fig. 5a). In addition, all samples had at least three size bins in the <0.6 mm range for which population density increased with decreasing size. Individual portions of the CSD can be separated for characterization, and so the slope and intercept of the <0.6 mm size range was considered here to compare CSDs of all samples (Table 3).

The two textural regions in 70275,35 exhibited distinct ilmenite CSD profile slopes and y-intercepts (Fig. 5g). Combining these two datasets into one CSD generated a profile with slope and intercept identical within uncertainty to the dominant finer-grained texture. The combined CSD of 70275 was the steepest of the three CSDs because it combined the low population of large (>2 mm) ilmenite phenocrysts in the fine-grained region with the higher population density of intermediate size (0.6–2 mm) crystals of the coarse-grained region (Fig. 1d). Table 3 also presents reprocessed ilmenite CSD data from three Apollo 12 ilmenite basalts previously reported by O'Sullivan and Neal (2010).

Ilmenite CSDs were curved in all textural Type 1A basalts, and most textural Type 1B basalts, indicating varying growth conditions. The <0.6 mm population had CSD profiles that are steepest in rapidly cooled samples. Qualitatively, in this size range coarse-grained basalts had shallow CSD profiles and lower y-intercepts, reflecting larger

Table 2
Frequency distribution of 2D crystal lengths calculated using *CSDCorrections* (Higgins, 2000).

Sample	Number of 2D crystal lengths per size interval (mm)												Total
	0.0251–0.0398	0.0398–0.0631	0.0631–0.1000	0.100–0.158	0.158–0.251	0.251–0.398	0.398–0.631	0.631–1.000	1.00–1.58	1.58–2.51	2.51–3.98	3.98–6.31	
Ilmenite													
70135,64	*1*	6	43	104	160	172	89	55	12	*0*	*0*	*0*	642
71048,6	138	271	342	302	178	45	18	3	*1*	*0*	*0*	*0*	1298
74235,60	1027	913	612	189	56	16	4	*1*	*0*	*0*	*0*	*0*	2818
75015,52	4	5	20	32	48	49	60	40	25	10	4	*1*	298
70315,27	3	19	50	76	98	125	102	34	5	*0*	*0*	*0*	512
71557,7	11	32	47	64	89	80	48	8	4	*0*	*0*	*0*	383
75075,86	5	24	96	129	163	170	114	44	17	4	*0*	*0*	766
78575,10	*2*	20	56	93	155	228	195	48	13	*1*	*0*	*0*	811
70275,35	615	1413	2021	1766	1267	591	205	63	12	5	*0*	*0*	7958
70275,35 (C)*	15	56	86	95	79	49	26	6	*2*	*0*	*0*	*0*	414
70275,35 (F)*	121	324	467	442	291	133	34	7	3	*2*	*0*	*0*	1824
71035,32	26	81	157	161	160	130	78	19	6	*0*	*1*	*0*	819
71157,8	2132	1438	951	416	174	45	19	6	*0*	*0*	*0*	*0*	5181
77516,30	29	87	182	201	195	106	39	11	*2*	*0*	*1*	*0*	853
79516,9	451	654	646	359	217	79	30	12	*1*	*1*	*0*	*0*	2450
71509,5	6	5	16	24	33	32	20	7	4	*0*	*0*	*0*	147
74255,55	61	179	273	313	317	219	67	18	1	*1*	*0*	*0*	1449
74275,312	140	250	276	166	89	16	5	3	2	*0*	*0*	*0*	947
75115,4	72	121	159	151	126	56	23	3	2	*0*	*0*	*0*	713
79001,2187	5	43	80	113	100	72	26	5	0	*0*	*0*	*0*	444
Pyroxene													
70135,64	*0*	3	39	80	154	178	170	97	38	20	4	*0*	783
75015,52	*0*	8	19	57	88	144	155	175	90	23	*0*	*0*	759
70315,27	*0*	3	11	19	53	83	72	53	27	7	*2*	*0*	330
71557,7	4	6	17	35	78	88	56	38	6	2	*0*	*0*	330
75075,86	4	4	10	47	105	123	110	68	23	6	*1*	*0*	501
78575,10	*2*	13	41	123	255	441	389	212	37	*2*	*0*	*0*	1515
71035,32	34	80	175	295	372	286	158	52	10	*0*	*1*	*0*	1463
71509,5	*1*	3	6	15	36	35	14	10	3	*2*	*0*	*0*	125
74255,55	13	26	83	175	229	174	82	32	6	4	*0*	*0*	824
79001,2187	49	90	186	228	215	139	44	11	*1*	*0*	*0*	*0*	963
Armalcolite													
74235,60	382	293	230	87	38	15	*1*	*2*	*0*	*0*	*0*	*0*	1048
74275,312	31	76	114	67	26	7	6	*1*	*0*	*0*	*0*	*0*	328
Plagioclase													
70135,64	*0*	*0*	7	19	43	58	55	42	15	12	2	0	253
75015,52	*0*	*0*	1	14	30	53	73	87	73	45	10	3	389
70315,27	*0*	*0*	0	3	15	28	32	21	19	5	*2*	*0*	125
71557,7	*0*	*0*	4	9	14	21	24	15	12	2	*0*	*0*	101
75075,86	*0*	5	12	50	65	79	77	59	30	8	*2*	*0*	387
78575,10	*0*	*0*	9	18	59	64	90	79	53	15	*2*	*0*	389
71035,32	*1*	*2*	36	100	155	176	153	66	16	3	*0*	*0*	708
74255,55	*0*	*2*	44	107	145	101	74	29	11	7	*1*	*0*	521
79001,2187	4	31	114	146	120	70	27	12	*1*	*0*	*0*	*0*	525
Olivine													
71048,6	*0*	*2*	8	18	26	17	5	*1*	*0*	*0*	*0*	*0*	77
74235,60	*2*	5	9	33	58	61	19	7	*0*	*0*	*0*	*0*	194
71157,8	*0*	*1*	9	35	45	38	21	14	3	*0*	*1*	*0*	167
77516,30	*0*	*1*	5	7	18	30	13	6	*1*	*0*	*0*	*0*	81
79516,9	*0*	*0*	6	9	25	29	20	2	*0*	*0*	*0*	*0*	91
74275,312	*0*	*1*	24	198	257	110	20	4	*2*	*1*	*0*	*0*	617
75115,4	*0*	*1*	11	12	21	33	4	*1*	*0*	*0*	*0*	*0*	83

Italicized values are below the minimum threshold for subsequent CSD calculations.
* (F) and (C) are the "fine" and "coarse" regions, respectively.

Table 3
Crystal size distribution and spatial distribution pattern data for the Apollo 17 titaniferous mare basalts.

Sample	Area (mm^2)	Vol.%	SDP *R*-value	Shape	Slope1 <0.6 mm	int1	Slope2 >0.6 mm	int2	Res. time (days)	*Q*	R^2 shape
Ilmenite											
70135,64	114	14%	1.02	1:1.4:2.8	−6.98	5.70	n.a.	n.a.	123	0.003	0.85
71048,6	18	13%	1.13	1:3:10	−11.6	9.36	−5.40	5.89	74–159	4.1E−15	0.77
74235,60	15	3%	0.78	1:6:10	−21.9	11.4	n.a.	n.a.	39	3.0E−79	0.89
75015,52	161	9%	0.88	1:1.6:10	−2.90	2.28	−0.99	0.21	296–866	2.0E−10	0.84
70315,27	72	15%	1.05	1:1.4:2.4	−6.95	5.83	n.a.	n.a.	124	0.747	0.83
71557,7	34	14%	1.05	1:1.5:3.4	−7.47	6.49	n.a.	n.a.	115	0.048	0.76
75075,86	117	14%	1.02	1:1.3:8	−3.71	4.35	−1.55	2.28	231–555	7.6E−14	0.65
78575,10	136	14%	1.06	1:1.5:2.5	−5.17	5.19	−5.60	4.37	166–153	6.4E−05	0.86
70275,35	223	11%	1.04	1:5:10	−11.5	8.76	−3.41	3.41	74–252	n.d.	0.65
71035,32	67	12%	0.97	1:1.9:9	−6.10	6.06	−2.74	3.90	141–313	1.1E−16	0.80
71157,8	25	10%	0.73	1:2.5:10	−15.6	11.8	−3.12	4.56	55–275	n.d.	0.76
77516,30	39	12%	1.03	1:2.5:9	−7.51	7.27	−4.17	4.88	114–206	2.7E−06	0.75
79516,9	27	13%	1.05	1:3.6:10	−15.2	10.2	−4.31	4.79	56–199	3.6E−146	0.78
71509,5	34	10%	0.91	1:1.5:2	−9.81	5.94	n.a.	n.a.	87	0.278	0.66
74255,55	68	11%	1.05	1:1.6:10	-5.00	6.29	−3.17	4.90	172–271	5.5E−08	0.87
74275,312	11	11%	1.12	1:2.7:8	−16.9	10.3	−3.48	3.23	51–247	1.1E−25	0.66
75115,4	18	14%	1.12	1:1.8:9	−7.78	7.84	−4.34	5.81	110–198	6.2E−08	0.64
79001,2187	21	12%	1.06	1:2:10	−5.05	6.40	n.a.	n.a.	170	0.368	0.72
Plagioclase											
70135,64	114	14%	1.05	1:2:4.5	−3.51	3.57	−1.27	−0.04	132–365	0.0003	0.87
75015,52	161	25%	1.06	1:2.7:8	−1.47	1.68	n.a.	n.a.	316	0.095	0.66
70315,27	72	16%	1.03	1:1.5:3.6	−2.50	2.54	n.a.	n.a.	186	0.481	0.64
71557,7	34	17%	0.99	1:1.5:4	-2.60	3.11	n.a.	n.a.	179	0.801	0.72
75075,86	117	17%	1.03	1:2:3.4	−4.22	4.18	n.a.	n.a.	110	0.004	0.76
78575,10	136	20%	1.12	1:1.7:5.5	−2.03	2.52	n.a.	n.a.	229	0.121	0.77
71035,32	67	20%	1.09	1:1.8:10	−2.26	4.08	n.a.	n.a.	205	0.079	0.78
74255,55	68	13%	0.96	1:2.3:5.5	−7.35	6.08	−2.35	2.02	63–198	7.8E−23	0.76
79001,2187	21	14%	1.1	1:1.9:6	−9.16	7.83	−4.99	5.25	51–93	1.2E−07	0.84
Pyroxene											
70135,64	82	50%	1.17	1:1.5:3	-4.94	5.40	-2.15	2.32	81–185	2.2E−15	0.79
75015,52	161	38%	1.14	1:1.4:2.6	−3.33	3.93	n.a.	n.a.	120	0.52	0.76
70315,27	72	32%	0.91	1:1.7:3.8	−3.09	3.97	n.a.	n.a.	129	0.105	0.79
71557,7	34	33%	1.01	1:1.4:2.8	−5.26	5.76	n.a.	n.a.	76	0.182	0.75
75075,86	58	35%	1.05	1:1.7:6	−2.58	4.25	n.a.	n.a.	154	0.009	0.74
78575,10	136	44%	1.16	1:1.5:2	−6.92	6.53	n.a.	n.a.	58	0.459	0.86
71035,32	67	32%	1.01	1:1.6:3.2	−8.26	7.33	−5.76	5.99	48–69	3.6E−05	0.84
71509,5	18	20%	0.82	1:1.6:2.7	−6.64	6.03	n.a.	n.a.	60	0.075	0.74
74255,55	36	37%	1.04	1:1.5:3.2	−7.46	7.25	−1.61	0.65	53–247	8.4E−20	0.82
79001,2187	21	34%	1.01	1:1.5:3.8	−8.60	8.27	n.a.	n.a.	46	0.007	0.83
Olivine											
71048,6	18	4%	1	1:1.5:2.3	−12.2	6.73	n.a.	n.a.	632	0.585	0.73
74235,60	66	4%	0.75	1:1.3:2.1	−7.77	5.58	n.a.	n.a.	993	0.047	0.78
71157,8	25	10%	1.07	1:2.2:3	−7.61	6.22	n.a.	n.a.	1014	0.095	0.73
77516,30	39	5%	0.81	1:1.4:2.4	−6.90	4.86	n.a.	n.a.	1118	0.285	0.80
79516,9	27	7%	1	1:1.3:2.9	−4.79	4.70	n.a.	n.a.	1611	0.586	0.76
74275,312	107	7%	0.92	1:1.3:1.9	−12.8	7.49	−11.5	6.76	603–671	0.0001	0.89
75115,4	18	6%	1.13	1:1.2:1.8	−8.30	6.07	n.a.	n.a.	930	0.008	0.72
Armalcolite											
74235,60	15	4%	0.91	1:1:1	−73.7	−0.07	n.a.	n.a.	16–30	3.8E−36	0.51
74275,312	106	0.40%	0.82	1:1.7:3.2	−29.8	8.04	−12.7	4.60	38–68	7.0E−09	0.88

n.a.: not applicable; n.d.: not determined.
Vol.% = volume percent.
Slope1 & int1 = slope and intercept of CSD profile at <0.6 mm size range.
Slope2 & int2 = slope and intercept of CSD profile at >0.6 mm size range.
Res. Time = calculated residence time (see text for details).
Q = *CSDCorrections* calculated goodness of fit of CSD profile to a straight line.
R^2 = Goodness of fit for the calculated shape parameters.

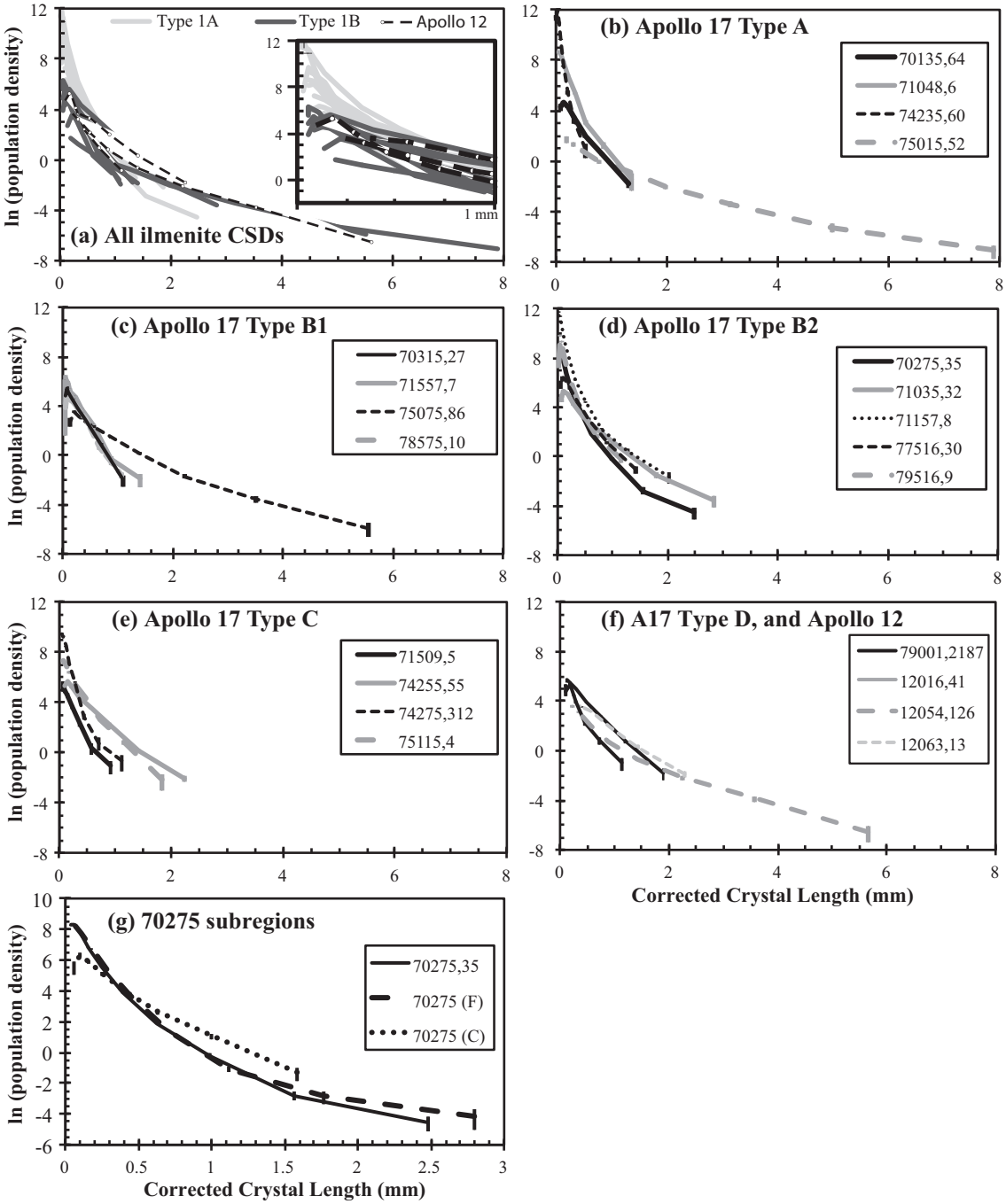

Fig. 5. (a) Ilmenite CSD profiles for all investigated samples, with distinctions between major textural groups and Apollo 12 basalts from O'Sullivan and Neal (2010). Inset of (a) is truncated at 1 mm size bin. (b-f) Ilmenite CSDs separated by chemical type. (b) Apollo 17 Type A basalts, (c) Apollo 17 Type B basalts, (d) Apollo 17 Type B1 basalts, (e) Apollo 17 Type C basalts, (f) Apollo 17 Type D basalt 79001 and Apollo 12 basalts, and (g) Type B2 70275,35 ilmenite CSDs for the entire section compared to the fine "F" and coarse "C" textural subregions discussed in the text.

overall crystal sizes but lower population densities. The <0.6 mm population was interpreted to be representative of post-emplacement crystallization and allowed comparison between samples of all textures. These relationships were made clearer by calculating the slope and intercept for the <0.6 mm population (Table 3; Fig. 6a). As indicated previously, slow-cooled textural Type 1B basalts delineated a field (dashed region of Fig. 6a) with distinctly lower nucleation density compared to faster-cooled textural Type 1A basalts. Uncertainties in slope and intercept values of Fig. 6 were calculated from the minimum and maximum population densities given in *CSDCorrections*, and were

typically smaller than symbol size shown. Ilmenite CSD data reported by Day and Taylor (2007) for low-Ti (3.1–3.4 wt.% TiO_2; Joy et al., 2006; Elardo et al., 2014) LaPaz basalts are also shown.

4.2. Olivine CSDs

Olivine CSD profiles from whole-rock Types A and B2 were linear (Fig. 7a and b), with Type A slopes (−12.2 and −7.7) steeper than Type B2 slopes (−7.6 to −4.9). Whole-rock Type C basalt 75115 had a sub-linear CSD profile, and the profile of Type C basalt 74275,312 was concave up (Fig. 7a). The total number of olivine crystals traced in each thin section varied from 77 to 198, with the exception of 74275,312 (617 crystals). However, the equant morphology of olivine met the requirements for >75 crystals per thin section, although the low number of crystals likely contributed to the low confidence for the estimated 3D shapes (R^2 of 0.72–0.80).

4.3. Plagioclase CSDs

Plagioclase CSD profiles (Fig. 7c and d) were concave up for samples 70135, 79001, and 74255 (listed in order of increasing degree of curvature). Phenocryst populations had slopes of −1.3 to −5.0 and intercepts of −0.04 to 5.3. Microphenocryst segments had slopes of −3.5 to −9.2 and intercepts of 3.6 to 7.8. The remaining samples were linear to sub-linear with slopes of −1.5 to −4.2 and intercepts of 1.7 to 4.2, similar to phenocryst populations from the curved CSDs.

4.4. Pyroxene CSDs

The majority of pyroxene CSD profiles were linear to sub-linear (Fig. 7e-f), indicating a relatively simple cooling history that allowed us to consider them each as a function of their slope and intercept. These arrays had slopes between −2.6 and −8.6 and intercepts between 3.9 and 8.3. Three non-linear CSDs (70135, 71035, 74255) were concave up to varying degrees. A convenient way to quantify these CSDs was to consider separately the population of large (phenocrysts) and small (microphenocrysts) crystals, splitting the CSD at an appropriate size (0.5–1 mm here). Phenocryst profile segments had slopes between −1.6 and −5.8 and intercepts between 0.65 and 6.0. Microphenocryst profiles had slopes of −4.9 to −8.3 and intercepts of 5.4 to 7.3.

4.5. Armalcolite CSDs

The two armalcolite CSD profiles were concave up and steep (Fig. 7g, Table 3). Both samples had larger size bins with fewer than three crystals and these were excluded from CSD calculations. The CSDs were split between "large" and "small" populations at ~0.1 mm. The CSD profile of the small size population of 74235,60 was steep with a slope and intercept of −73.7 and −0.07. The large population of 74235,60 had a similar slope and intercept to the small population of whole-rock Type C basalt 74275,312. The large population of 74275,312 had a slope and intercept of −12.7 and 4.6.

5. DISCUSSION

5.1. Cooling rates and residence times

Cooling rates of the groundmass can be interpreted as being dependent on where the basalts crystallized within a flow. Textures of Apollo 17 high-Ti basalts were previously reproduced in cooling-rate studies of high-Ti basalt analogues (Usselman et al., 1975; Usselman and Lofgren, 1976), and the results were used to estimate cooling rates for basalts 74235 (150–250 °C/h), 74275 (5–10 °C/h), 74255 (1–3 °C/h), and 75075 (<1 °C/h). These four basalts cover the range of textures used to calculate CSD slopes and intercepts (except for 75015,52; Fig. 6). All textural Type 1B basalts can be tied to cooling rates below ~3 °C/h. Texture, CSD slope, CSD intercept, and cooling rate are essentially independent of bulk chemistry.

The groundmass ilmenite texture and resulting CSD profile can be largely interpreted as being a function of location within a lava flow (*cf.* Day and Taylor, 2007). However, sub-ophitic low-Ti samples 12016,41 and LAP 02436,18 plot contrarily in the region of faster cooling (Fig. 6a). The noted relationship between texture and

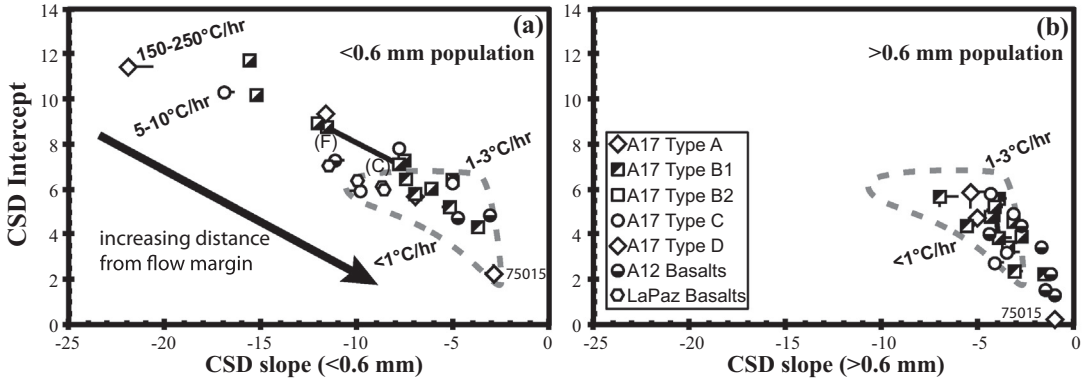

Fig. 6. The slope-intercept relationship for ilmenite CSD profiles of (a) <0.6 mm size bins and (b) >0.6 mm size bins. Dashed region in (b) encompasses all textural Type 1B basalts. Cooling rates of groundmass crystals from Usselman et al. (1975). (b) Ilmenite CSD slope-intercept relationship for >0.6 mm size bin population, with dashed region and cooling rates as in (a).

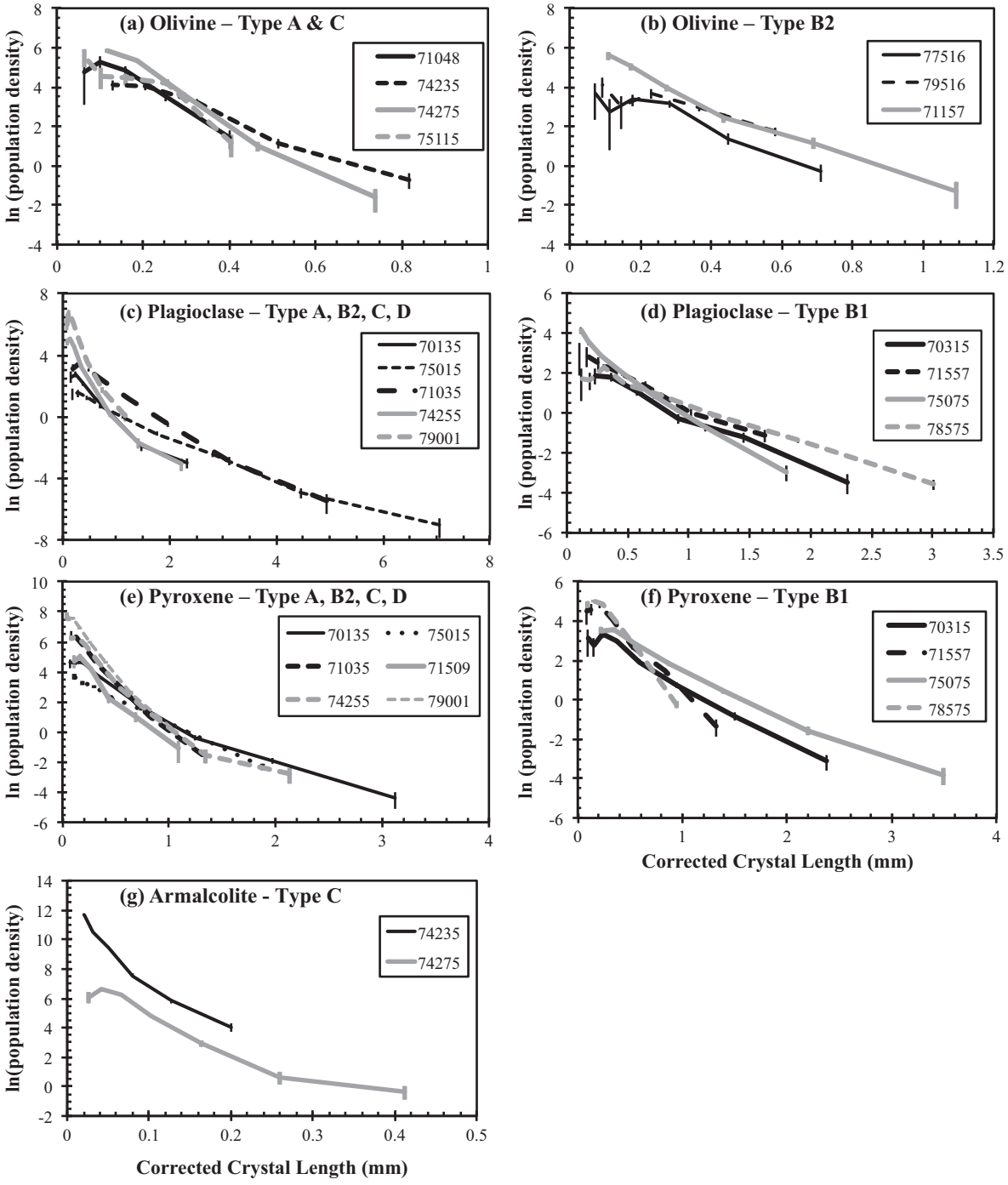

Fig. 7. CSDs of other major phases in Apollo 17 high-Ti basalts. Olivine CSDs of (a) whole-rock Type A and C basalts and (b) Type B2 basalts are all linear to sub-linear and separated for clarity. Plagioclase CSDs of (c) Types A, B2, C, and D have variable slopes, and (d) Type B1 plagioclase CSDs are all (sub)-linear. Pyroxene CSDs of (e) Type A, B2, C, and D basalts and (f) Type B1 basalts are separated for clarity. (g) Armalcolite CSDs were determined for Type A basalt 74235,60 and Type C basalt 74275,312 only. Vertical bars represent the minimum and maximum range in calculated population density.

stratigraphy may only hold for high-Ti basalts, where ilmenite is on the liquidus for a longer period of time. Another possibility is that ilmenite is a late stage, interstitial phase in many low-Ti mare basalts, and surrounding phases interfere with growth. This would result in CSDs that reflect atypical crystallization conditions for growth and residence time.

Residence times can be calculated for a given CSD slope if the phase growth rate is known. Ilmenite growth rate and nucleation density decrease over time and at lower

temperatures (Burkhard, 2005), both of which are variable in the high-Ti basalt suite. For experimentally determined growth rates (1.35×10^{-8} mm/s) of basaltic Fe–Ti oxides (Burkhard, 2005), residence times of groundmass ilmenite range from ~39 days (for 74235) to ~300 days (for 75015) (Table 3). The textural variation in 70275 indicates a cooling rate change of up to several degrees per hour at the scale of the thin section. At growth rates noted above, groundmass residence time in 70275 varies from 70 to 110 days. These coarse regions may be trapped microcosms of melt that were insulated to allow slower cooling, or they may also be entrained packages of slower cooled basaltic melt carried or settled into a fast-cooling zone.

Ilmenite CSD profiles of some samples are linear (as for whole-rock Type A 70315 and whole-rock Type D 79001,2187), indicating crystallization under relatively constant conditions. However, CSD profiles are concave up for many textural Type 1B basalts and for all fine-grained textural Type 1A basalts. Using the method applied to the <0.6 mm populations (Fig. 6a), analysis of the populations >0.6 mm yield comparatively lower CSD slopes and intercepts. Indeed, the textural Type 1A and 1B basalts are no longer distinguishable when considering the >0.6 mm population (Fig. 6b). Slope-intercept relationships indicate this population of larger ilmenite crystals formed at cooling rates of <3 °C/h (Fig. 6b). For most samples this requires crystallization prior to eruption, supporting petrographic observations and experimental work that high-Ti mare basalts erupted with ilmenite on the liquidus (e.g., Usselman and Lofgren, 1976). Curved CSDs can also result from textural coarsening, whereby small crystals are lost at the expense of preferential growth of large crystals. While this may have affected certain coarse-grained samples (e.g., 75015), it is not a factor in the curvature of textural Type 1A basalts cooling at rates above a few degrees per hour, which would have cooled too quickly for any coarsening to occur. Residence times for phenocryst ilmenite range from 60 to 860 days. Note that the residence times calculated from >0.6 mm portions of CSD profiles in 70275,35 are similar between the "fine-grained" region (220 days), "coarse-grained" region (210 days), and whole sample CSD profiles (250 days).

Pyroxene and plagioclase CSDs of textural Type 1B basalts can be used to place additional timing constraints on these coarse-grained samples. Similarly, olivine and armalcolite CSDs may aid our understanding of the textural Type 1A basalts. In the study noted above, Burkhard (2005) also determined growth rates for plagioclase (2.49×10^{-8} mm/s) and pyroxene (2.91×10^{-8} mm/s) at the same conditions as for ilmenite. Plagioclase crystals have residence times of 51–365 days, and pyroxene crystals have residence times of 46–247 days (Table 3). Armalcolite growth rates are taken to be the same as ilmenite, and armalcolite residence times for the two samples range from 16 to 30 days for 74235,60 and 40–70 days for 74275,312. In both cases, armalcolite has a shorter residence time than for ilmenite, as armalcolite became unstable as crystallization proceeded, as indicated by mantles of ilmenite on some crystals. Olivine growth rates of 1.5×10^{-9} (Vinet and Higgins, 2010) are an order of magnitude smaller than other phases and have longer residence times of 600–1100 days, but we note that all of these phases did not crystallize simultaneously. Olivine and armalcolite are replaced by pyroxene and ilmenite (respectively) in the crystallization sequence of mare basalts (e.g., Papike et al., 1974, 1976; Haskin and Korotev, 1977). The presence of large olivine crystals in a fine-grained groundmass requires crystallization prior to eruption, supported by the longer residence times calculated here.

5.2. Relative stratigraphy

Individual volcanic regions around the Apollo 17 region were active over time frames on the order of tens to hundreds of millions of years, sufficient to fill the Taurus-Littrow Valley with ~2 km of mare basalt (Paces et al., 1991; Jolliff et al., 2006). Ilmenite residence times of, at most, a few years point to rapid magma generation and eruption resulting in brief periods of volcanism (e.g., Paces et al., 1991), or that ilmenite had a short crystallization window in some high-Ti basalts. The thickness and number of individual flows in the valley is masked by regolith, which is estimated to be <25 m thick by the active seismic experiment (Kovach et al., 1973; Kovach and Watkins, 1973a,b). The conclusion from this experiment was that the Taurus-Littrow landing site was underlain by a layered structure, inferred to be 1200 m of mare basalts. At least five separate events are required to generate the geochemical groups in the sample collection (Neal et al., 1990; Paces et al., 1991). Here, matrix ilmenite is used to place samples in context of a flow profile, similar to observations of terrestrial flood basalts by Thordarson and Self (1998). However, the type of basaltic flow must first be determined as on Earth there are two main types – pahoehoe and a'a. Cashman et al. (1999) noted that Hawaiian lavas flows transitioned from pahoehoe to a'a once a rheological transition had been reached. Sato (1995) concluded that initial melting temperature controlled the number of plagioclase nuclei with a'a lavas resulting from slightly lower melting temperatures than pahoehoe, which led to a larger number of plagioclase crystallization nuclei that produced higher yield strengths. Katz and Cashman (2003) used plagioclase crystallinity to describe the difference between pahoehoe and a'a flows (see their Fig. 2) when the number of plagioclase crystals per mm^2 (N_a) is plotted against plagioclase volume fraction crystallized (Φ_P). All Apollo 17 samples plot below the pahoehoe and Makaopuhi Lava Lake samples (Fig. 8) because mare basalts have lower viscosities than terrestrial basalts (e.g., Murase and McBirney, 1970). The only exception is the sole representative of the whole-rock Type D grouping (79001,2187), which plots with the terrestrial pahoehoe lavas (Fig. 8). The results indicate the Apollo 17 high-Ti basalts were emplaced as pahoehoe flows.

Pahoehoe lava flows are considered to thicken through inflation as more lava is pumped along a conduit, which produces a distinctive stratigraphy (e.g., Hon et al., 1994; Self et al., 1996, 1998; Thordarson and Self, 1998). In the investigation of lava flow stratigraphy, models of pahoehoe inflation can be used here. Fig. 9 is a schematic representation of an inflated pahoehoe flow with the Apollo 17 high-Ti basalt samples placed in a relative stratigraphy

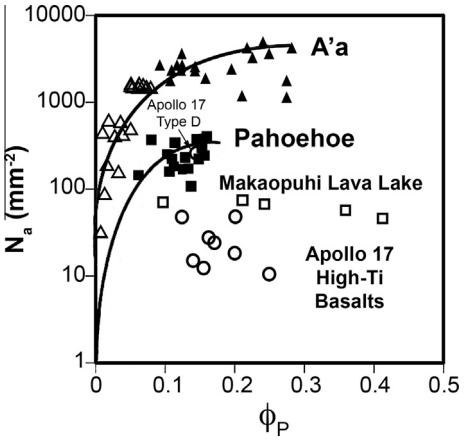

Fig. 8. Plot of plagioclase number densities (N_a in number/mm^2) as a function of plagioclase volume fraction crystallized (ϕ_P) measured in Apollo 17 high-Ti mare basalts. Modified from Katz and Cashman (2003). A'a = triangles, pahoehoe = squares; Apollo 17 basalts = circles. Data for Hawaiian lavas from Katz and Cashman (2003) and references therein.

based upon texture and relative cooling rate as determined in this study. The pahoehoe flow is subdivided into three zones on the basis of vesicle structures, jointing, and crystallinity (Self et al., 1998; Thordarson and Self, 1998), which are from bottom to top: the lower crust (20–100 cm thick irrespective of flow thickness, vesicles are distributed throughout, crystallinity is hypohyaline to hypocrystalline); core (very few vesicles, holocrystalline); and the upper crust (40–60% of the lobe, discrete horizontal vesicular zones that form due to inflation separated by more massive lava, with crystallinity varying from hypohyaline to hypocrystalline). Given that the Apollo 17 basalts were not sampled in situ (i.e., were distributed across the lunar surface via impacts) it is not surprising that the basalts studied here contained very few vesicles because vesicular zones would not have survived the impact zone. However, textures and cooling rates indicate that not all samples came from the core section of the flows. Some likely came from the more rapidly cooled upper crust where vesicle poor zones exist (Fig. 9; Self et al., 1998; Thordarson and Self, 1998). Whole-rock Type A basalts 74235 and 75015 represent the fine and coarse textural end-members, respectively. The remaining samples are ordered based on ilmenite morphology, groundmass texture, and cooling rates and residence times calculated here. The base of the chilled top in Fig. 9a marks the transition zone from textural Type 1A to Type 1B. A one-meter thick lava flow would cool to have a center typified by the texture of basalt 74255 (Usselman et al., 1975), suggesting a minimum thickness for coarser textured samples.

Phenocryst textural characteristics may be useful in determining whether samples began crystallizing in near-surface environments. Ilmenite is the only phase that allows comparison between all high-Ti basalt geochemical types. Splitting the ilmenite CSD at 0.6 mm distinguishes between phenocryst and groundmass ilmenite crystal populations. Using the slope and intercept of the CSD at <0.6 mm, the findings of Usselman et al. (1975) have been expanded to include cooling rates and residence times for all investigated Apollo 17 basalts.

Initial-Sr isotope values have been reported for many of the samples investigated here and are used in conjunction with CSD slope values to discriminate between derivation from different source regions and, therefore, eruption in separate flows (Fig. 10a and b). The results for whole-rock

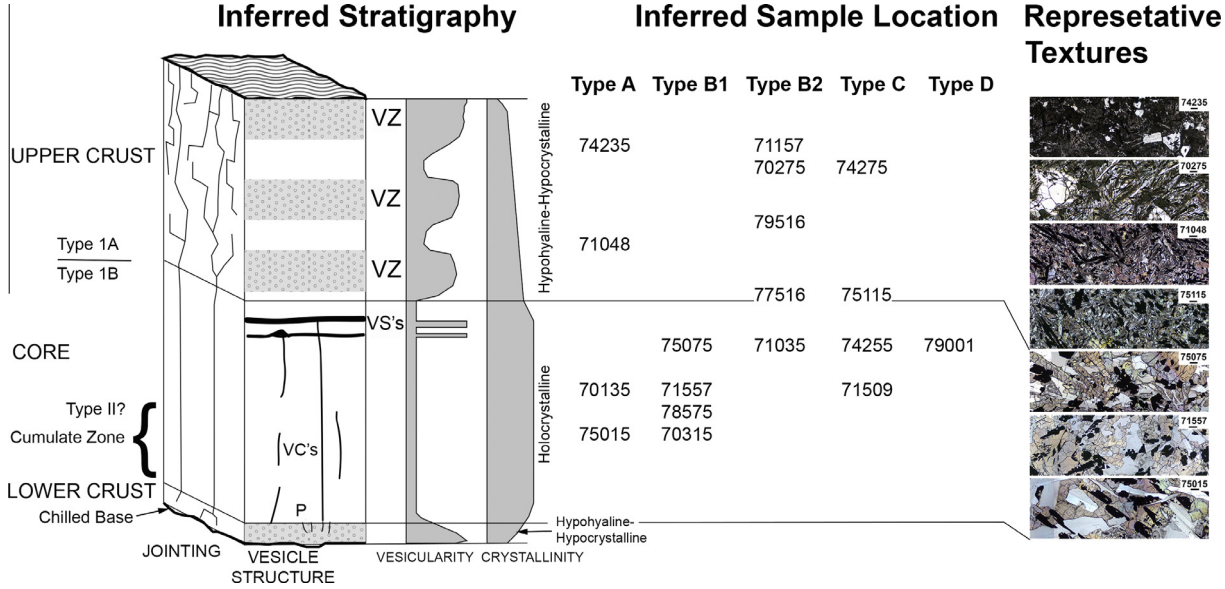

Fig. 9. A schematic model of an inflated pahoehoe flow (modified from Self et al., 1998) and the relative positions of the different basalt samples studied here are shown, along with representative textures. Highlighted in the column is the division between the different textural types (1A, 1B, and II). Samples are listed by whole-rock chemical type for Apollo 17 in inferred relative positions of occurrence, although it is not inferred that they are from a single flow. P = Pipes; VC's = Vesicle Cylinders; VS's = Vesicle Sheets; VZ = Vesicular Zone.

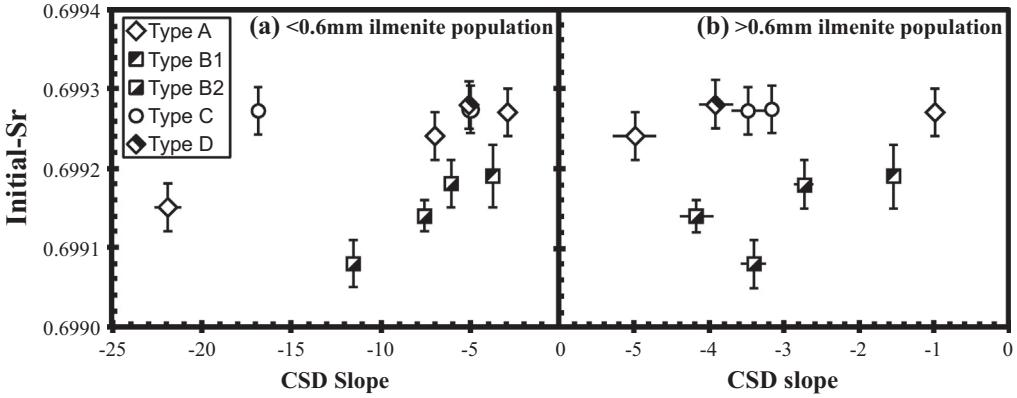

Fig. 10. Ilmenite CSD profile slope versus calculated Initial-Sr from literature bulk-rock analyses for (a) <0.6 mm portion of CSD profiles, and (b) >0.6 mm portion of CSD profiles. (Literature data from Lugmair, 1975; Lugmair et al., 1975; Nyquist et al., 1975, 1976; Murthy and Coscio, 1976; Nyquist, 1977; Unruh et al., 1984; Paces et al., 1991; Dasch et al., 1998).

Type C basalts 72455 and 74275 show that they cooled on the surface at different rates, as reflected in their matrix ilmenite CSD characteristics and their overall textures. However, they have identical phenocryst ilmenite textures and initial-Sr values (Fig. 10b), supporting at least derivation from a similar source, if not a co-magmatic origin, then followed by crystallization in different parts of the lava flow. Whole-rock Type A basalt 74235, on the other hand, may have originated from a separate source region and, therefore, from a separate volcanic event from other Type A basalts 70135 and 75015. Additional isotopic data for Apollo 17 basalts would aid in defining the relative timing of regions of activity.

6. CONCLUSIONS

The results of this textural analytical study have shown that ilmenite records the thermal history of high-Ti mare basalts for a range of textural varieties, from olivine microporphyritic to plagioclase poikilitic. In particular, groundmass ilmenite populations reflect the degree of textural coarsening in a sample as a function of cooling rate. The groundmass and phenocryst populations were ascribed to varying residence times and were used to build a lava flow profile for the five chemical suites of high-Ti basalt. The textural investigation of olivine supported their pre-eruption growth (months to years), timescales matched only by some of the larger phenocryst ilmenite populations. Pyroxene and plagioclase are defined by uninterrupted growth and cooling rates in plagioclase poikilitic (textural Type 1B) basalts as a result of their single-stage growth history. These new textural relationships provide a link between the Apollo samples and experimental studies, place these samples within the stratigraphy of a lava flow, and quantify the cooling rates of high-Ti mare basalts.

ACKNOWLEDGEMENTS

The authors thank NASA Johnson Space Center for the loan of thin sections and the creation of new thin section 71157,8. We also thank Jeff Taylor and Katherine Joy for their thoughtful reviews, and Marc Norman and Wolf Uwe Reimold for editorial handling. This research was supported by NASA Cosmochemistry grant NNX09AB92G to CRN.

REFERENCES

Brown G. M., Peckett A., Emeleus C. H., Phillips R. and Pinsent R. H. (1975) Petrology and mineralogy of Apollo 17 mare basalts. In *Proc. Lunar Sci. Conf. 6*th. pp. 1–13.

Burkhard D. J. M. (2005) Nucleation and growth rates of pyroxene, plagioclase, and Fe–Ti oxides in basalt under atmospheric conditions. *Eur. J. Mineral.* **17**, 675–686.

Cashman K. V. and Marsh B. D. (1988) Crystal size distribution (CSD) in rocks and the kinetics and dynamics of crystallization II: Makaopuhi lava lake. *Contrib. Mineral. Petrol.* **99**, 292–305.

Cashman K. V., Thornber C. and Kauahikaua J. P. (1999) Cooling and crystallization of lava in open channels, and the transition of pahoehoe to a'a. *Bull. Volcanol.* **61**, 306–323.

Dasch J., Ryder G., Reese Y., Wiesmann H., Shih C.-Y. and Nyquist L. (1998) Old age of formation for a distinct variety of A17 high-titanium mare basalt. *Lunar Planet. Sci. Conf. XXIX*, #1750 (abstr.).

Day J. M. D. and Taylor L. A. (2007) On the structure of mare basalt lava flows from textural analysis of the LaPaz Icefield and Northwest Africa 032 lunar meteorites. *Meteorit. Planet. Sci.* **42**, 3–17.

Donohue P. H. (2013) Origin and evolution of high-titanium mare basalts. Unpub. Ph. D. dissertation, Univ. Notre Dame, 173 p.

Dymek R. F., Albee A. L. and Chodos A. A. (1975) Comparative mineralogy and petrology of Apollo 17 mare basalts: Samples 70215, 71055, 74255, and 75055. In *Proc. Lunar Sci. Conf. 6*th. pp. 49–77.

Elardo S. M., Shearer, Jr, C. K., Fagan A. L., Borg L. E., Gaffney A. M., Burger P. V., Neal C. R., Fernandes V. A. and McCubbin F. M. (2014) The origin of young mare basalts inferred from lunar meteorites Northwest Africa 4734, 032, and LaPaz Icefield 02205. *Meteorit. Planet. Sci.* **49**, 261–291.

Fagan A.L. and Neal C.R. (2012) Apollo 11-type basalts from Apollo 16: A new type of high-Ti basalt? *43rd Lunar Planet. Sci. Conf.*, Houston, TX. #1429 (abstr.).

Fagan A.L. and Neal C.R. (2014) A new basalt type from Apollo 16. *Geochim. Cosmochim. Acta* (under revision).

Fagan A. L., Neal C. R., Simonetti A., Donohue P. H. and O'Sullivan K. M. (2013) Distinguishing between Apollo 14 impact melt and pristine mare basalt samples by geochemical

and textural analyses of olivine. *Geochim. Cosmochim. Acta* **106**, 429–445.
Haskin L. A. and Korotev R. L. (1977) Test of a model for trace element partition during closed-system solidification of a silicate liquid. *Geochim. Cosmochim. Acta* **41**, 921–939.
Higgins M. D. (2000) Measurement of crystal size distributions. *Am. Mineral.* **85**, 1105–1116.
Higgins M. D. (2006) Verification of ideal semi-logarithmic, lognormal or fractal crystal size distributions from 2D datasets. *J. Volcanol. Geotherm. Res.* **154**, 8–16.
Hon K., Kauahikaua J. P., Denlinger R. and McKay K. (1994) Emplacement and inflation of pahoehoe sheet flows: Observations and measurements of active lava flows on Kilauea Volcano, Hawaii. *Geol. Soc. Amer. Bull.* **106**, 351–379.
Hui H., Oshrin J. G. and Neal C. R. (2011) Investigation into the petrogenesis of Apollo 14 high-Al basaltic melts through crystal stratigraphy of plagioclase. *Geochim. Cosmochim. Acta* **75**, 6439–6460.
Jerram D. A., Cheadle M. J., Hunter R. H. and Elliott M. T. (1996) The spatial distribution of grains and crystals in rocks. *Contrib. Mineral. Petrol.* **125**, 60–74.
Jerram D. A., Cheadle M. J. and Philpotts A. R. (2003) Quantifying the building blocks of igneous rocks: Are Clustered crystal frameworks the foundation? *J. Petrol.* **44**, 2033–2051.
Jerram D. A., Davis G. R., Mock A., Charrier A. and Marsh B. D. (2010) Quantifying 3D crystal populations, packing and layering in shallow intrusions: A case study from the Basement Sill, Dry Valleys, Antarctica. *Geosphere* **6**, 537–548.
Jolliff B. L., Hughes J. M., Freeman J. J. and Zeigler R. A. (2006) Crystal chemistry of lunar merrillite and comparison to other meteoritic and planetary suites of whitlockite and merrillite. *Am. Mineral.* **91**, 1583–1595.
Joy K. H., Crawford I. A., Downes H., Russell S. S. and Kearsley A. T. (2006) A petrological, mineralogical, and chemical analysis of the lunar mare basalt meteorite LaPaz Icefield 02205, 02224, and 02226. *Meteorit. Planet. Sci.* **41**, 1003–1025.
Katz M. G. and Cashman K. V. (2003) Hawaiian lava flows in the third dimension: Identification and interpretation of pahoehoe and a'a distribution in the KP-1 and SOH-4 cores. *Geochem. Geophys. Geosyst.* **4**, 8705. http://dx.doi.org/10.1029/2001GC000209.
Kovach R.L. and Watkins J.S. (1973a) The structure of the lunar crust at the Apollo 17 site. In *Proc. Lunar Sci. Conf. 4*th. pp. 2549–2560.
Kovach R. L. and Watkins J. S. (1973b) Apollo 17 seismic profiling: Probing the lunar crust. *Science* **180**, 1063–1064.
Kovach R.L., Watkins J.S., and Talwani P. (1973) Lunar seismic profiling experiment. In *Apollo 17 Prelim. Sci. Rpt.*, Chapter 10, Lyndon B. Johnson Space Center NASA SP-330. 12 p.
Lugmair G. W. (1975) Sm–Nd systematics of some Apollo 17 basalts. *Conf. Origin Mare Basalts Implic. Lunar Evol.*, 107–109.
Lugmair G. W., Scheinin N. B. and Marti K. (1975) Sm–Nd age and history of Apollo 17 basalt 75075: Evidence for early differentiation of the lunar exterior. In *Proc. Lunar Sci. Conf. 6*th. pp. 1419–1429.
Marsh B. D. (1988) Crystal size distribution (CSD) in rocks and the kinetics and dynamics of crystallization I. Theory. *Contrib. Mineral. Petrol.* **99**, 277–291.
Marsh B. D. (1998) On the interpretation of crystal size distributions in magmatic systems. *J. Petrol.* **39**, 553–599.
Martin V. M., Pyle D. M. and Holness M. B. (2006) The role of crystal frameworks in the preservation of enclaves during magma mixing. *Earth Planet. Sci. Lett.* **248**, 787–799.
Meyer C. (1994) Catalog of Apollo 17 Rocks, Volume 4 – North Massif. NASA Lyndon B. Johnson Space Center, JSC# 26088. 584 p.
Morgan D. J. and Jerram D. A. (2006) On estimating crystal shape for crystal size distribution analysis. *J. Volcanol. Geotherm. Res.* **154**, 1–7.
Murase T. and McBirney A. R. (1970) Viscosity of lunar lavas. *Science* **167**, 1491–1493.
Murthy V. R. and Coscio M. R. Jr. (1976) Rb-Sr ages and isotopic systematics of some Serenitatis mare basalts. In *Proc. Lunar Sci. Conf. 7*th. pp. 1529–1544.
Neal C. R. and Taylor L. A. (1992) Petrogenesis of mare basalts: A record of lunar volcanism. *Geochim. Cosmochim. Acta* **56**, 2177–2211.
Neal C. R. and Taylor L. A. (1993a) Catalog of Apollo 17 Rocks, volume 1: Stations 2 and 3 (North Massif). NASA Lyndon B. Johnson Space Center, JSC #26088. 379 p.
Neal C. R. and Taylor L. A. (1993b) Catalog of Apollo 17 Rocks, volume 2: Central Valley, Part 1. NASA Lyndon B. Johnson Space Center, JSC# 26088. 472 p.
Neal C. R. and Taylor L. A. (1993c) Catalog of Apollo 17 Rocks, volume 3: Central Valley, Part 2. NASA Lyndon B. Johnson Space Center, JSC# 26088. 291 p.
Neal C. R., Taylor L. A., Hughes S. S. and Schmitt R. A. (1990) The significance of fractional crystallization in the petrogenesis of Apollo 17 Type A and B high-Ti basalts. *Geochim. Cosmochim. Acta* **54**, 1817–1833.
Nyquist L. E. (1977) Lunar Rb–Sr chronology. *Phys. Chem. Earth* **10**, 103–142.
Nyquist L. E., Bansal B. M. and Wiesmann H. (1975) Rb–Sr ages and initial $^{87}Sr/^{86}Sr$ for Apollo 17 basalts and KREEP basalt 15386. In *Proc. Lunar Sci. Conf. 6*th. pp. 1445–1465.
Nyquist L. E., Bansal B. M. and Wiesmann H. (1976) Sr isotopic constraints on the petrogenesis of Apollo 17 mare basalts. In *Proc. Lunar Sci. Conf. 7*th. pp. 1507–1528.
O'Sullivan K. M. (2012) Petrogenesis of planetary basalts using crystal stratigraphy. Thesis, University of Notre Dame, 190 p.
O'Sullivan K. M. and Neal C. R. (2010) Exploring the petrogenesis of Apollo 12 Ilmenite Suite basalts. *Lunar Planet. Sci. Conf.* **41**, #2322 (abstr.).
Paces J. B., Nakai S., Neal C. R., Taylor L. A., Halliday A. N. and Lee D.-C. (1991) A strontium and neodymium isotopic study of Apollo 17 high-Ti mare basalts: Resolution of ages, evolution of magmas, and origins of source heterogeneities. *Geochim. Cosmochim. Acta* **55**, 2025–2043.
Papike J. J., Bence A. E. and Lindsley D. H. (1974) Mare basalts from the Taurus-Littrow region of the moon. *Proc. Lunar Conf. 5th* **1**, 471–504.
Papike J. J., Hodges F. N., Bence A. E., Cameron M. and Rhodes J. M. (1976) Mare basalts: Crystal chemistry, mineralogy, and petrology. *Rev. Geophys. Space Phys.* **14**, 475–540.
Rasband W. S. (1997) ImageJ. *imagej.nih.gov*. Available at: http://imagej.nih.gov/ij/ (Accessed 2013).
Rhodes J. M., Hubbard N. J., Wiesmann H., Rodgers K. V., Brannon J. C. and Bansal B. M. (1976) Chemistry, classification, and petrogenesis of Apollo 17 mare basalts. In *Proc. Lunar Sci. Conf. 7*th. pp. 1467–1489.
Ryder G. (1990) A distinct variant of high-titanium mare basalt from the Van Serg core, Apollo 17 landing site. *Meteorit.* **25**, 249–258.
Ryder G. (1992) Catalog of Apollo 17 Rocks, volume 1 – Stations 2 and 3 (South Massif). NASA Lyndon B. Johnson Space Center, JSC# 26088. 379 p.
Sato H. (1995) Textural difference between pahoehoe and a'a lavas of Izu-Oshima volcano, Japan; an experimental study on

population density of plagioclase. *J. Volcanol. Geotherm. Res.* **66**, 101–113.

Self S., Thordarson Th., Keszthelyi L., Walker G. P. L., Hon K., Murphy M. T., Long P. and Finnemore S. (1996) A new model for the emplacement of Columbia River basalts as large, inflated pahohoe lava flows. *Geophys. Res. Lett.* **23**, 2689–2692.

Self S., Keszthelyi L. and Thordarson Th. (1998) The importance of pahoehoe. *Annu. Rev. Earth Planet. Sci.* **26**, 81–110.

Shearer C. K. Jr., Papike J. J., Galbreath K. C., Yurimoto H. and Shimizu N. (1990) Secondary ion mass spectrometric analysis of glasses, trace element characteristics of lunar picritic glasses and implications for the mantle sources of lunar picritic magmas. *Workshop on Lunar Volcanic Glasses: Scientific and Resource Potential*, 58–59.

Thordarson T. and Self S. (1998) The Roza Member, Columbia River Basalt Group: A gigantic pahoehoe lava flow field formed by endogenous processes? *J. Geophys. Res.* **103**, 27411–27445.

Unruh D. M., Stille P., Patchett P. J. and Tatsumoto M. (1984) Lu-Hf and Sm-Nd evolution in lunar mare basalts. *J. Geophys. Res.* **89**, B459–B477.

Usselman T. M. and Lofgren G. E. (1976) The phase relations, textures, and mineral chemistries of high-titanium mare basalts as a function of oxygen fugacity and cooling rate. In *Proc. Lunar Sci. Conf. 7*th. pp. 1345–1363.

Usselman T. M., Lofgren G. E., Donaldson C. H. and Williams R. J. (1975) Experimentally reproduced textures and mineral chemistries of high-titanium mare basalts. In *Proc. Lunar Sci. Conf. 6*th. pp. 997–1020.

Vinet N. and Higgins M. D. (2010) Magma Solidification Processes beneath Kilauea Volcano, Hawaii: A Quantitative Textural and Geochemical Study of the 1969–1974 Mauna Ulu Lavas. *J. Petrol.* **51**, 1297–1332.

Warner R. D., Keil K., Murali A. V. and Schmitt R. A. (1975a) Petrogenetic relationships among Apollo-17 basalts. In *Conf. Origin Mare Basalts Implic. Lunar Evol.* pp. 179–183.

Warner R. D., Keil K., Prinz M., Laul J. C., Murali A. V. and Schmitt R. A. (1975b) Mineralogy, petrology, and chemistry of mare basalts from Apollo 17 rake samples. In *Proc. Lunar Sci. Conf. 6*th. pp. 193–220.

Warner R. D., Taylor G. J., Conrad G. H., Northrop H. R., Barker S., Keil K., Ma M. S. and Schmitt R. A. (1979) Apollo 17 high-Ti mare basalts: New bulk compositional data, magma types, and petrogenesis. In *Proc. Lunar Planet. Sci. Conf. 10th*. pp. 225–247.

Zeigler R. A., Korotev R. L., Haskin L. A., Jolliff B. L. and Gillis J. J. (2006) Petrography and geochemistry of five new Apollo 16 mare basalts and evidence for post-basin deposition of basaltic material at the site. *Meteorit. Planet. Sci.* **41**, 263–284.

Associate editor: Wolf Uwe Reimold